Eleventh International Conference on Computational Fluid Dynamics (ICCFD11), Maui, Hawaii, U.S.A., July 11-15, 2022

ICCFD11-2022-4201

On the Simulation of Statistically Unsteady Flows with the RANS Equations

L.Eça*, M.Kerkvliet** and S.L.Toxopeus**
Corresponding author: luis.eca@ist.utl.pt
* IST ULisbon, Portugal.
** MARIN, The Netherlands.

Abstract: Many engineering applications are still based on the solution of the Reynolds-Averaged Navier-Stokes (RANS) equations that require the definition of mean flow quantities and the averaging of the continuity and momentum equations. Most RANS turbulence models available in the open literature have been developed for statistically steady flows, i.e. time-averaging is applied to the flow variables and to the continuity and momentum equations. In external flows around bluff bodies or large angles of incidence in streamlines bodies, wide wakes are generated due to massive flow separation and vortex shedding will occur. In such conditions, time-averaging is not a reasonable option for the definition of the mean flow, because time variations generated by the vortex shedding phenomena will be considered as turbulence fluctuations. As for the statistically steady flows, the role of the Reynolds stresses is to damp the turbulence fluctuations and allow the determination of the mean flow. However, there is no guarantee that turbulence models developed for time-averaged RANS will also be appropriate for statistically unsteady flows.
In this paper, we present simulations for the flow around a circular cylinder at Reynolds numbers ranging from sub-critical (transition in the near-wake) to super-critical (transition on the cylinder upstream of separation) performed with three turbulence models: the Shear-Stress Transport (SST) $k-\omega$ two-equation eddy-viscosity model, an explicit algebraic Reynolds Stress model (EARSM) based on a SST $k-\omega$ and a Reynolds Stress model (RSM). Two-dimensional and three-dimensional approaches are compared and the contribution of statistical, iterative and discretization errors to the numerical uncertainty are estimated for all flow conditions. With this simple flow, we assess if the turbulence model is able to provide the required diffusion to damp turbulence fluctuations and allow the determination of the mean flow solution.

Keywords: Computational Fluid Dynamics, RANS, Statistically Unsteady flows, Numerical errors.

1 Introduction

Modeling and Simulation (MS) has become an essential part of Engineering. One of the branches of MS that is routinely used is Computational Fluid Dynamics (CFD), that can address a wide variety of flows including different types of physical phenomena. One of the challenges of CFD is the accurate simulation of turbulent flows that occur in many practical applications. Currently, it is possible to simulate turbulent flows solving numerically mass conservation and momentum balance (Navier-Stokes equations) without any extra modeling (Direct Numerical Simulation, DNS). However, the requirements to perform such simulations in complex geometries at high Reynolds numbers are unaffordable. Therefore, many engineering applications are still based on the solution of the Reynolds-Averaged Navier-Stokes (RANS) equations that require the definition of mean flow quantities and the averaging of the continuity and momentum equations. This results in additional terms in the momentum equations, the so-called Reynolds stresses that require a turbulence model for their determination.

Most RANS turbulence models available in the open literature have been developed for statistically steady flows, see for example Wilcox [1], i.e. time-averaging is applied to the flow variables and to the continuity and momentum equations. The extra diffusion provided by the Reynolds stress tensor is supposed to provide enough diffusion to damp all turbulence fluctuations and enable the calculation of a mean steady flow.

In external flows around bodies of arbitrary shape, statistically steady flows require streamlined shapes aligned with the incoming flow, i.e. boundary-layers that do not exhibit significant flow separation. For bluff bodies or large angles of incidence in streamlines bodies, wide wakes are generated due to massive flow separation and vortex shedding will occur. In such conditions, time-averaging is not a reasonable option to calculate the mean flow, because time variations generated by the vortex shedding phenomena will be considered as turbulence fluctuations. In these statistically unsteady flows, the derivation of the RANS equations is based on ensemble averaging and so the time derivatives of the mean flow quantities are not zero, which is usually referred to as (U)nsteady RANS. As for the statistically steady flows, the role of the Reynolds stresses is to damp the turbulence fluctuations and allow the determination of the mean flow. However, there is no guarantee that turbulence models developed for time-averaged RANS will also be appropriate for statistically unsteady flows.

In this paper, we present RANS based simulations for the flow around a circular cylinder at Reynolds numbers ranging from sub-critical, $Re = 3.9 \times 10^3$ and $Re = 10^5$ (transition in the near-wake) to super-critical $Re = 3.6 \times 10^6$ and $Re = 10^8$ (transition on the cylinder upstream of separation), performed with two-dimensional and three-dimensional approaches using three different turbulence models: the Shear-Stress Transport (SST) $k{-}\omega$, two-equation, eddy-viscosity model [2]; the explicit algebraic Reynolds Stress model (EARSM) based on a $k{-}\omega$ model [3]; the SSG/LRR-ω full Reynolds stress model (RSM) [4]. The dimensions of the circular cylinder and computational domain are based on [5] that reports experimental data for two of the selected Reynolds numbers.

The aim of the present paper is twofold:

1. Evaluate the different contributions to the numerical uncertainty in unsteady RANS simulations;

2. Assess if the selected turbulence models are able to provide the required diffusion to damp turbulence fluctuations.

As discussed in [6], unsteady flow simulations can be affected by round-off, iterative, discretization and statistical errors. The estimation of the contributions of these errors to the numerical uncertainty is essential to quantify modeling errors [7]. On the other hand, if the selected turbulence models do not provide sufficient damping, the dependent variables of the ensemble-averaged RANS equations will no longer be the mean flow variables and their meaning will be difficult to interpret. In this study, we analyse the frequency content of the time histories of integral and near-wake local flow quantities to assess if the solution determines the mean flow field. These two aspects of the simulation of statistically unsteady turbulent flows with the RANS equations are connected because numerical errors can provide extra diffusion to the simulations and influence its outcome.

The assessment of numerical errors in unsteady flow simulations may be time consuming, especially in three-dimensional geometries. Therefore, we have also included in this study the simulation of the flow around two-dimensional and three-dimensional circular cylinders for a Reynolds number of $Re = 100$ that corresponds to laminar flow. This simple flow allows an easier estimation of the numerical uncertainty and so its purpose is to illustrate the challenges of such task for turbulent flows.

The remainder of this paper is organized the following way: the mathematical model is presented in section 2 and the problem definition including geometry, flow settings and boundary conditions in section 3; the flow solver and the numerical details are described in section 4, whereas section 5 presents and discusses the results; the main conclusions are summarized in section 6.

2 Mathematical Model

Flows of incompressible fluids are governed by mass conservation and momentum balance, which can be expressed in a Cartesian coordinate system as

$$
\begin{gathered}
\frac{\partial \tilde{V}_i}{\partial x_i} = 0, \\
\frac{\partial \left(\tilde{V}_i\right)}{\partial t} + \frac{\partial \left(\tilde{V}_i \tilde{V}_j\right)}{\partial x_j} = -\frac{1}{\rho}\frac{\partial \tilde{P}}{\partial x_i} + \frac{1}{\rho}\frac{\partial \tau_{ij}}{\partial x_j} \ ,
\end{gathered}
\tag{1}
$$

where $\tilde{V}_i$ are the Cartesian velocity components, ρ is the fluid density, $\tilde{P}$ is the relative pressure[1] and τ_{ij} are the components of the stress tensor, which for a Newtonian fluid are given by:

$$
\frac{\tau_{ij}}{\rho} = \nu \left(\frac{\partial \tilde{V}_i}{\partial x_j} + \frac{\partial \tilde{V}_j}{\partial x_i} \right) \ , \tag{2}
$$

where ν is the kinematic viscosity of the fluid.

At high Reynolds numbers the flows are always three-dimensional and unsteady due to the existence of turbulence. Flow variables exhibit fluctuations in a wide range of frequencies that make the direct solution of equations (1) unaffordable.

2.1 Reynolds Averaged Navier-Stokes (RANS) Equations

To simulate complex engineering applications, the Reynolds averaged Navier-Stokes (RANS) turbulence models are commonly used. The derivation of the RANS equations from equations (1) include two steps:

1. Express the flow dependent variables $\tilde{\phi}$ as the sum of a mean value Φ and a fluctuating component ϕ;
2. Apply the averaging procedure to the mass and momentum balances equations.

In statistically steady flows, mean values Φ are obtained with time-averaging. However, in external flows including massive flow separation that leads to vortex shedding time-averaging becomes physically unsuitable. In such conditions, ensemble-averaging is used to define Φ

$$
\Phi(x_i, t) = \lim_{N \to \infty} \sum_{j=1}^{N} \frac{\tilde{\phi}_j(x_i, t)}{N} \ . \tag{3}
$$

Unlike time-averaging, the mean value obtained from ensemble-averaging depends on time.

Applying ensemble-averaging to mass conservation, momentum balance and to the flow dependent variables we obtain the Reynolds-averaged continuity and momentum equations,

$$
\begin{gathered}
\frac{\partial V_i}{\partial x_i} = 0, \\
\frac{\partial V_i}{\partial t} + \frac{\partial \left(V_i V_j\right)}{\partial x_j} = -\frac{1}{\rho}\frac{\partial P}{\partial x_i} + \frac{1}{\rho}\frac{\partial \tau_T}{\partial x_j} \ , \\
\frac{\tau_T}{\rho} = \nu \left(\frac{\partial V_i}{\partial x_j} + \frac{\partial V_j}{\partial x_i} \right) - \overline{v_i v_j}
\end{gathered}
\tag{4}
$$

V_i and P are the mean values of the Cartesian velocity components and pressure, respectively. v_i are the fluctuating part (turbulence) of the Cartesian velocity components and the overbar designates averaging. The Reynolds stress tensor $-\rho\overline{v_i v_j}$ is generated by the two steps of the averaging procedure and requires a turbulence model to close the problem.

[1] Reference pressure is the hydrostatic pressure.

2.1.1 Turbulence Models

The SST $k-\omega$, two-equation eddy-viscosity model [2] is based on the so-called Boussinesq approximation that determines the Reynolds stress tensor as a function of the mean strain rate and the eddy-viscosity ν_t

$$-\overline{v_i v_j} = \nu_t \left(\frac{\partial V_i}{\partial x_j} + \frac{\partial V_j}{\partial x_i} \right) - \frac{2}{3}\delta_{ij} k \ , \tag{5}$$

where k is the turbulence kinetic energy and δ_{ij} is the Kronecker symbol. The contribution of k to the normal stresses is absorbed in the mean pressure gradient term and so the RANS equations (4) become similar to the original equations (1) with two main changes:

- the dependent variables are ensemble-averaged quantities;
- dynamic viscosity of the fluid is replaced by the effective viscosity $\nu_{\text{eff}} = \nu + \nu_t$.

The SST $k-\omega$ model solves two extra transport equations for k and for the specific turbulence dissipation ω and determines ν_t from k and ω and a limiter based on the Bradshaw hypothesis [2].

The Explicit Algebraic Reynolds Stress model (EARSM) proposed in [3] adds an anisotropic contribution $a_{ij}^{(ex)}$ to the Reynolds stress tensor calculated from equation (5). The model also solves transport equations for k and ω that define the value of the eddy-viscosity. $a_{ij}^{(ex)}$ is calculated from algebraic expressions based on the mean strain rate and vorticity tensors.

The SSG/LRR-ω Reynolds-Stress model (RSM) proposed in [4] solves seven transport equations to determine six components of the Reynolds stress tensor (the tensor is symmetric) and ω. Therefore, this model does not rely on the eddy-viscosity to determine the Reynolds stresses. Nonetheless, the model still requires the calculation of the eddy-viscosity to solve the ω transport equation.

It must be mentioned that equations (4) are similar to the equations of Large-Eddy Simulation (LES). However, the dependent variables of the LES equations are filtered quantities and the unknown residual stress tensor generated by the filtering process can be interpreted as the sum of three tensors and only one of them is similar to the Reynolds stress tensor. Nonetheless, there are several LES model that also use the eddy-viscosity approach to obtain the so-called subgrid scale model. This means that in the absence of sufficient diffusion, the numerical solution of equations (4) will solve flow features that do not belong to the mean flow field.

3 Problem Definition

The flow around a circular cylinder of diameter D is the the problem addressed in this study. The ratio between the length of the cylinder axis L and D is set equal to $L/D = 50/15$ to match the conditions reported in [5]. The center of the cylinder is located at the origin of the Cartesian coordinate system illustrated in figure 1 and the computational domain is a parallelepiped with three pairs of parallel faces and length of $120D$ (x direction), height of $12D$ (y direction) and width of $3.33D$ (z direction).

Five Reynolds numbers based on the velocity of the uniform incoming flow V_∞, D and ν are tested: $Re = 100$, $Re = 3.9 \times 10^3$, $Re = 10^5$, $Re = 3.6 \times 10^6$ and $Re = 10^8$. $Re = 100$ corresponds to laminar flow, $Re = 3.9 \times 10^3$ and $Re = 10^5$ are in the sub-critical regime with laminar flow separation on the cylinder surface and transition to turbulence in the near-wake and $Re = 3.6 \times 10^6$ and $Re = 10^8$ are in the super-critical regime with transition to turbulence in the attached boundary-layer on the surface of the cylinder and separation in the turbulent boundary-layer [8]. The choice of the lowest Re is justified by the need to include a Re that facilitates the evaluation of numerical errors. $Re = 3.9 \times 10^3$ is one of the Re with more published results for the flow around a circular cylinder [9]. $Re = 10^5$ and $Re = 3.6 \times 10^6$ have experimental data available in [5] and $Re = 10^8$ can be easily attained in aquaculture applications [10].

The difference between two and three-dimensional simulations is just the number of cells used in the transverse z direction, which is equal to 1 for two-dimensional simulations.

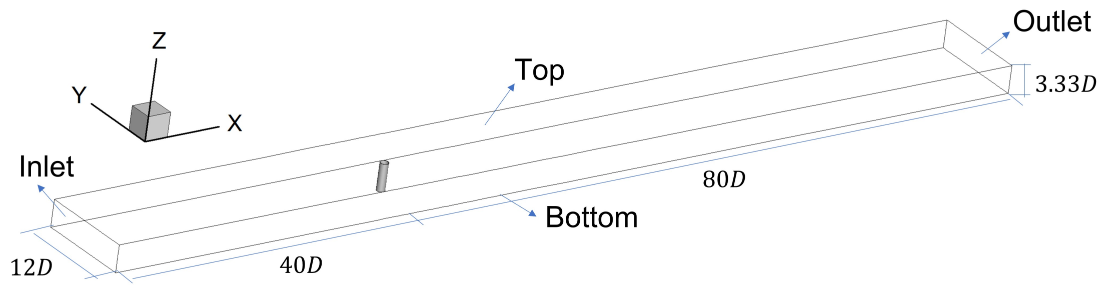

Figure 1: Illustration of the computational domain for the simulation of the flow around a circular cylinder.

3.1 Boundary Conditions

The following boundary conditions are applied at the seven boundaries of the computational domain:

- At the inlet boundary ($x = -40D$), the mean velocity components are set equal to $V_x = V_\infty$, $V_y = V_z = 0$ and the pressure is extrapolated from the interior of the domain. The turbulence kinetic energy k and the normal Reynolds stresses are derived from a turbulence intensity $I = v_x/V_x = 0.007$ [5] assuming isotropic turbulence. The value of ω is calculated from k and ν_t using the empirical relation[2] $(\nu_t/\nu)_{\text{inlet}} = 10^{-8}Re$.
- Pressure is imposed at the outlet plane ($x = 80D$) and the derivatives with respect to x of all remaining dependent variables are set equal to zero.
- At the top ($y = 6D$) and bottom ($y = -6D$) boundaries free slip conditions are imposed. Therefore, $V_y = 0$, Reynolds shear-stresses in the normal direction are set equal to zero and derivatives with respect to y of the remaining dependent variables are set equal to zero.
- Symmetry conditions are applied at the lateral boundaries of the domain ($z = 0$ and $z = 3.33D$). Naturally, in the two-dimensional simulations the momentum equation in the transverse z direction is not solved and $V_z = 0$.
- On the cylinder surface, the no-slip and impermeability conditions impose mean velocity components, turbulence kinetic energy and Reynolds stresses equal to zero. On the other hand, for a smooth wall ω tends to infinity at the wall [1]. In the present simulations, ω is specified at the cell center of the near-wall cells [11] using the near-wall analytic solution of the ω transport equation [1]. The shear-stress at the wall τ_w is calculated directly from its definition for all Reynolds numbers tested.

4 Flow Solver and Numerical Details

4.1 Flow Solver

All simulations were performed with ReFRESCO that is a flow solver based on a finite volume discretization of the continuity and momentum equations written in strong conservation form. The solver uses a fully-collocated arrangement and a face-based approach that enables the use of cells with an arbitrary number of faces. Picard linearization and mass conservation is ensured using a SIMPLE-like algorithm, [12], and a pressure-weighted interpolation technique to avoid spurious oscillations, [13]. Time integration is performed with implicit schemes and so a non-linear problem must be solved at each time step. In the

[2]Based on authors experience.

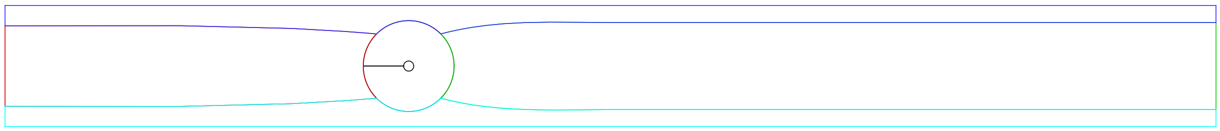

Figure 2: Illustration of the grids topology in the $x-y$ plane. Three-dimensional grids are obtained by extruding the two-dimensional $x-y$ grids in the transverse direction z.

Table 1: Number of cells N_{cells}, number of faces around the circular cylinder N_θ, number of faces along the transverse direction N_z and grid refinement ratio h_i/h_1 of the grid sets used in the two-dimensional (2D) and three-dimensional (3D) simulations performed for the flow around a circular cylinder at several Reynolds numbers (Re).

Grid	$10^2 \leq Re \leq 10^5$		$3.6\times10^6 \leq Re \leq 10^8$		$10^2 \leq Re \leq 10^8$			
	N_{cells}		N_{cells}		N_θ	N_z		h_i/h_1
	2D	3D	2D	3D	2D/3D	2D	3D	2D/3D
4	6,624	158,976	11,232	269,568	192	1	24	2.67
3	11,776	376,831	19,968	638,976	256	1	32	2
2	26,496	1,271,808	44,928	2,156,544	384	1	48	1.33
1	47,104	3,014,656	79,872	5,111,808	512	1	64	1
F1	95,984	*10,174,464*	179,712	*17,252,352*	768	1	*96*	0.67
F2	188,416	*24,117,248*	319,488	*40,894,464*	1024	1	*128*	0.5

present study, a segregated approach was adopted for all simulations, which means that momentum, pressure correction (mass conservarion) and turbulence equations are solved sequentially for each non-linear iteration. Thorough code verification is performed for all releases of ReFRESCO, [14].

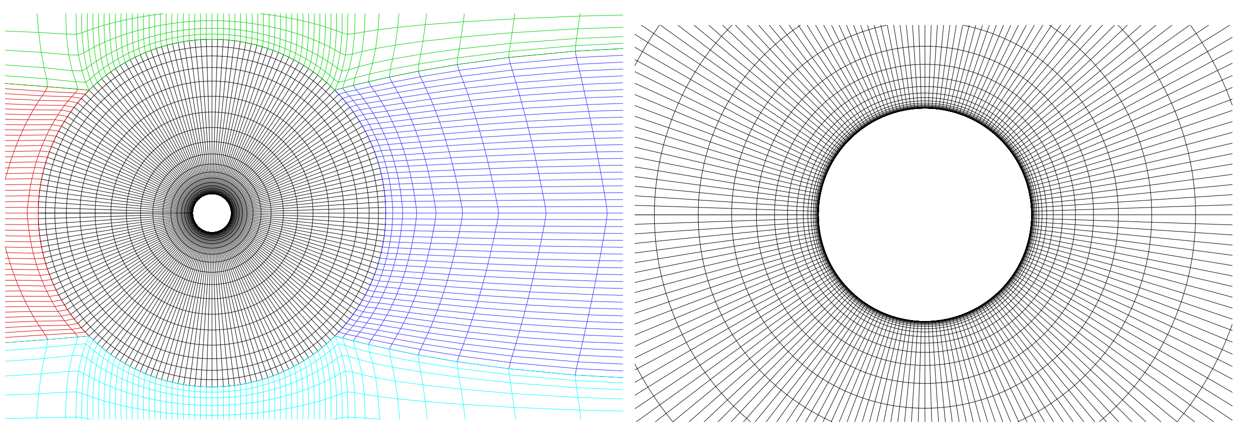

Figure 3: Illustration of the coarsest grid for the calculation of the flow around the circular cylinder.

4.2 Grid Sets

Sets of multiblock geometrically similar grids were generated with the algebraic, hyperbolic and elliptic grid generation tools described in [15]. The grids topology in the $x-y$ plane is illustrated in figure 2 and a view of the coarsest grid in the vicinity of the cylinder for $Re = 10^8$ is presented in figure 3. The angle θ of the polar coordinates in the $x-y$ plane is $\theta = 0°$ at $x = -D/2, y = 0$ and $\theta = \pm180°$ at $x = D/2, y = 0$.

The cell faces on the cylinder surface along θ have the same size and the stretching functions proposed by Vinokur [16] are used to define the cell sizes along the boundaries of the remaining blocks. Longitudinal cell sizes at the inlet and outlet are increased to avoid pressure reflections. The three-dimensional grids are obtained by extruding the $x - y$ grid along the transverse direction using a constant cell width along z. Two-dimensional simulations are performed with only one cell in the transverse direction.

Table 1 presents the total number of cells N_{cells}, the number of faces around the circular cylinder N_θ, the number of faces along the transverse direction N_z and the grid refinement ratio h_i/h_1 of all the grid sets used in this study. The grids F1 and F2 were used only for the 2D simulations due to the resources required to perform the 3D simulations in these grids. This option is a consequence of the iterative convergence criteria adopted for this study. More details are presented below. As a consequence, the reference cell size h_1 corresponds to the finest grid used in the three-dimensional simulations for all Reynolds numbers. For the turbulent flow simulations, the maximum non-dimensional height of the near-wall of cells in wall coordinates on the cylinder surface is approximately 0.7 for the coarsest grids of all the Reynolds numbers tested. Naturally, this value decreases with grid refinement.

4.3 Discretization Techniques

Second-order schemes are applied to the space and time discretization of all transport equations, including k, ω and Reynolds stresses transport equations. However, flux limiters are applied to the convective terms of all equations. Non-orthogonality and eccentricity corrections are applied to diffusion and convection discretization schemes. For the selected grid topology, these corrections are only active more than $4.5D$ away from the cylinder surface.

4.4 Solution Strategy

The solution strategy has a significant influence on the statistical convergence of the flow simulations. For all flow settings used in this study, the calculations were started by the simulations in the grid with $h_i/h_1 = 2$ using an initial condition copied from the inflow conditions and a loose iterative convergence criteria at each time step that corresponds to the L_∞ norm of the normalized residual of 10^{-3} for the momentum and pressure correction equations. The simulation time of these initial computations is sufficient to start the vortex shedding phenomena.

The time step of the following simulations is selected to obtain a maximum Courant number below 3 in the simulations performed with the adopted iterative convergence criteria. For the 2D simulations, at least 24 cycles are calculated with the time-averaged results obtained from the last 10 cycles. On the other hand, for three-dimensional simulations at least 48 cycles are simulated and 20 cycles are used to obtain the time-averaged solution. A cycle is the time interval between two consecutive time instants that exhibit a lift coefficient equal to zero with a slope larger than zero.

For the remaining grids, the initial condition is obtained by interpolating the solution obtained in the final time step of the closest grid refinement level available. The time step is changed with the same ratio used for the grid refinement, which means that the grid/time refinement studies are performed for an approximately constant Courant number. Naturally, the three turbulence models used in this study will not lead exactly to the same Courant numbers for a fixed time step. Nonetheless, the largest values of the Courant number are equal to approximately 2.8 for $Re = 3.9 \times 10^3$. The average Courant number is smaller than 0.5 for all the flow simulations performed in this study.

As explained, the proportional time step is selected by

$$r_i = \frac{h_i}{h_1} = \frac{\Delta t_i}{\Delta t_1}$$

and so discretization errors can be estimated with the procedure proposed in [17].

4.5 Iterative Convergence Criteria

The iterative convergence criteria tol_{it} used at each time step is based on the L_∞ norm of the normalized residuals of the momentum and pressure correction equations. Normalized residuals correspond to dimensionless variables changes in a simple Jacobi iteration.

5 Results

5.1 Quantities of Interest

The selected quantities of interest for this study include functional (integral), surface and local flow quantities. The lift C_L and drag C_D coefficients are the functional flow quantities, for which we have determined the time histories and the time-averaged values. The surface quantities are the time-averaged distributions of pressure coefficient C_p and skin friction coefficient C_f on the cylinder surface defined by

$$C_p = \frac{p - p_{\text{ref}}}{\frac{1}{2}\rho V_\infty^2} \text{ and } C_f = \frac{\tau_w}{\frac{1}{2}\rho V_\infty^2} \, .$$

The reference pressure p_{ref} is the maximum value of the pressure at the inlet of the computational domain. For three-dimensional simulations, time-averaged C_p and C_f distributions are interpolated at $z = 0.5L = 1.67D$ and also averaged along the transverse direction z, $(C_p)_z$ and $(C_f)_z$. In the results presented below C_f is multiplied by $0.5\sqrt{Re}$.

The location of flow separation θ_{sep} on the upper and lower surface of the cylinder is defined by the sign change of the shear-stress x-component. As for C_p and C_f, θ_{sep} is determined at $z = 0.5L = 1.67D$ and averaged along the transverse direction $(\theta_{\text{sep}})_z$. The time histories of the mean velocity components V_x, V_y and V_z are determined for point P_1 located at $x = 0.75D, y = 0.4D, z = 1.66D$ using second-order interpolation techniques.

Naturally, for a flow that exhibits vortex shedding, we have also determined the Strouhal number,

$$St = \frac{fD}{V_\infty} \, ,$$

with the shedding frequency f obtained from the first harmonic of the C_L time evolution.

5.2 Numerical Errors

All simulations were performed in double precision (14 digits) and so it is assumed that the contribution of round-off errors to the numerical uncertainty is negligible.

5.2.1 Statistical Errors

The simulation time should be sufficiently long to reduce the influence of the initial flow condition to negligible levels and achieve a statistically converged flow. As illustrated in figure 4, for simple flows as the present test case at $Re = 10^2$, it is not troublesome to assess statistical convergence. However, the estimation of statistical errors may pose significantly challenges when the frequency content of the time histories of the dependent variables is not as simple as that depicted in figure 4.

Although there are more sophisticated techniques to assess statistical convergence available, see for example [18, 19], we have calculated four quantities that are supposed to statistically converge to zero:

1. the time-averaged C_L coefficient;

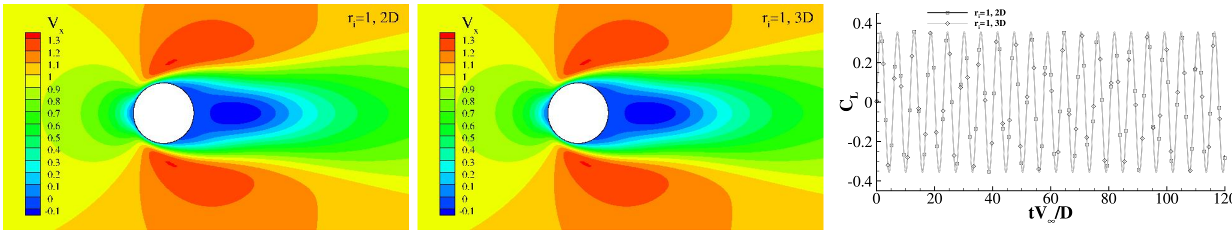

Figure 4: Time history of the lift coefficient C_L and isolines of time-averaged mean axial velocity V_x at $z = 0.5L = 1.67D$ obtained in the grids with $r_i = 1$ in two-dimensional and three-dimensional simulations of the flow around the circular cylinder at a Reynolds number of $Re = 10^2$.

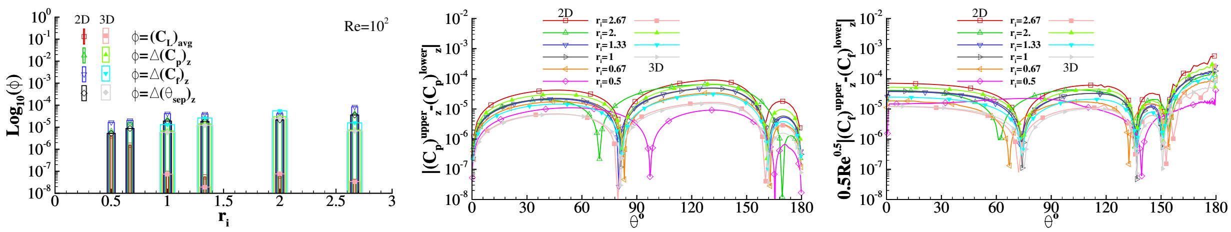

Figure 5: Assessment of statistical convergence from the symmetry of the time-averaged flow field obtained for different values of the grid/time refinement ratio, r_i. Average lift coefficient $(C_L)_{\text{avg}}$, differences between transverse averaged pressure $\Delta(C_p)_z$ and skin friction $\Delta(C_f)_z$ coefficients and flow separation location $\Delta(\theta_{\text{sep}})_z$ on the upper and lower surfaces of the cylinder surface. Calculation of the flow around the circular cylinder at a Reynolds number of $Re = 10^2$.

2. the average difference between the time C_p and transverse averaged $(C_p)_z$ pressure coefficients on the upper and lower surface of the cylinder, ΔC_p and $\Delta(C_p)_z$, respectively;

3. the average difference between the time C_f and transverse averaged $(C_f)_z$ skin friction coefficients on the upper and lower surface of the cylinder, ΔC_f and $\Delta(C_f)_z$, respectively;

4. the sum of the transverse averaged flow separation angles $(\theta_{\text{sep}})_z$ from the upper and lower surfaces of the cylinder, $\Delta(\theta_{\text{sep}})_z$.

Naturally, for 2D simulations there is no need to average on the transverse direction because there is only one cell in the transverse direction. On the other hand, the calculation of $\Delta(C_p)_z$ and $\Delta(C_p)_f$ for the 3D simulations does not require any interpolation because all grids used in this study are symmetric with respect to $y = 0$. $\Delta(C_p)_z$, $\Delta(C_f)_z$ and $\Delta(\theta_{\text{sep}})_z$ are divided by reference quantities calculated from the average of the absolute values of these quantities. All the results presented in this section were calculated with $tol_{\text{it}} = 10^{-6}$.

Figure 5 illustrates these four quantities for all the simulations performed for $Re = 10^2$. The data confirms quantitatively the low level of statistical errors achieved for all simulations performed for the laminar flow around a circular cylinder. There is not a big influence of the level of grid/time refinement ratio r_i on the statistical convergence, which is similar for the 2D and 3D simulations.

Figure 6 presents the four variables that illustrate the statistical convergence of the simulations for all the turbulent flow simulations performed in this study. The main trends observed in the data are:

- With the exception of the two finest grids of the 2-D SST simulations at $Re = 3.9 \times 10^3$, all the simulations exhibit values smaller than 10^{-2} for the four selected variables. Strangely, the two exceptions are not caused by statistical convergence. These two simulations lead to asymmetric flow fields and so the selected flow variables do not tend to zero with the increase of the simulation time;

- In general, the 3D simulations exhibit large statistical errors than the 2D calculations. However, this trend can be a consequence of the frequency content of the mean flow variables obtained in the two types of simulations;

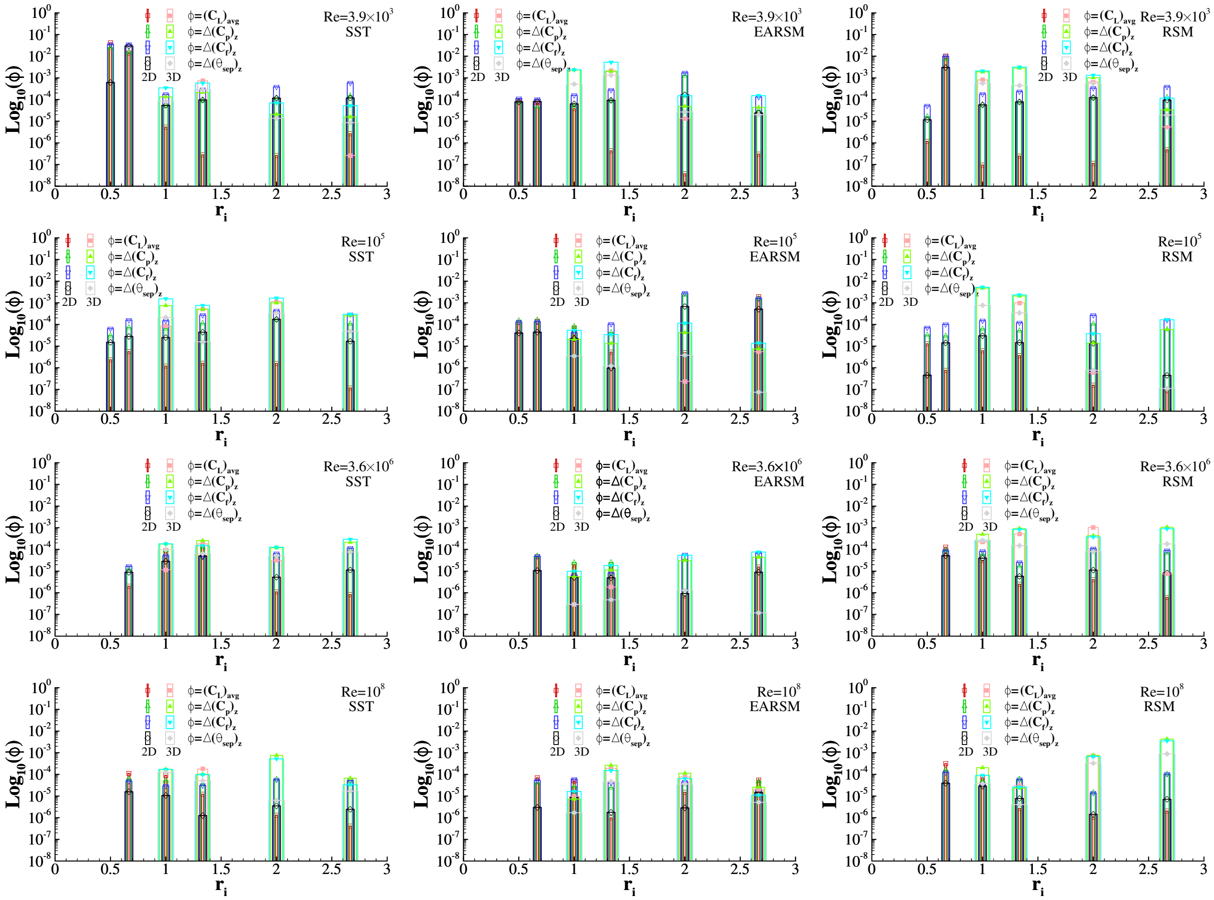

Figure 6: Assessment of statistical convergence from the symmetry of the time-averaged flow field obtained for different values of the grid/time refinement ratio, r_i. Average lift coefficient $(C_L)_{\text{avg}}$, differences between transverse averaged pressure $\Delta(C_p)_z$ and skin friction $\Delta(C_f)_z$ coefficients and flow separation location $\Delta(\theta_{\text{sep}})_z$ on the upper and lower surfaces of the cylinder surface. Calculation of the flow around the circular cylinder at Reynolds numbers of $Re = 3.9 \times 10^3$, $Re = 10^5$, $Re = 3.6 \times 10^6$ and $Re = 10^8$.

- The two lowest Reynolds numbers ($Re = 3.9 \times 10^3$ and $Re = 10^5$) show larger statistical errors than the two largest Reynolds numbers ($Re = 3.6 \times 10^6$ and $Re = 10^8$);
- There is no clear influence of the grid/time refinement on the level of the four selected flow quantities that quantify the symmetry of the time-averaged flow field. It is also difficult to identify any influence of the selected turbulence model on the outcome of the checking of the symmetry of the time-averaged flow fields.

Although the results presented in figure 6 are not sufficient to guarantee a negligible influence of statistical convergence on the numerical uncertainty of the flow variables analysed in this study, the main trends observed in the data obtained from the simulations should not be qualitatively affected by statistical convergence.

5.2.2 Iterative Errors

In flow solvers based on implicit time integration, a non-linear problem must be solved at each time step and so an iterative convergence criteria is required. As illustrated in [20], iterative errors may have a strong influence on the numerical uncertainty of unsteady flow simulations without affecting statistical convergence.

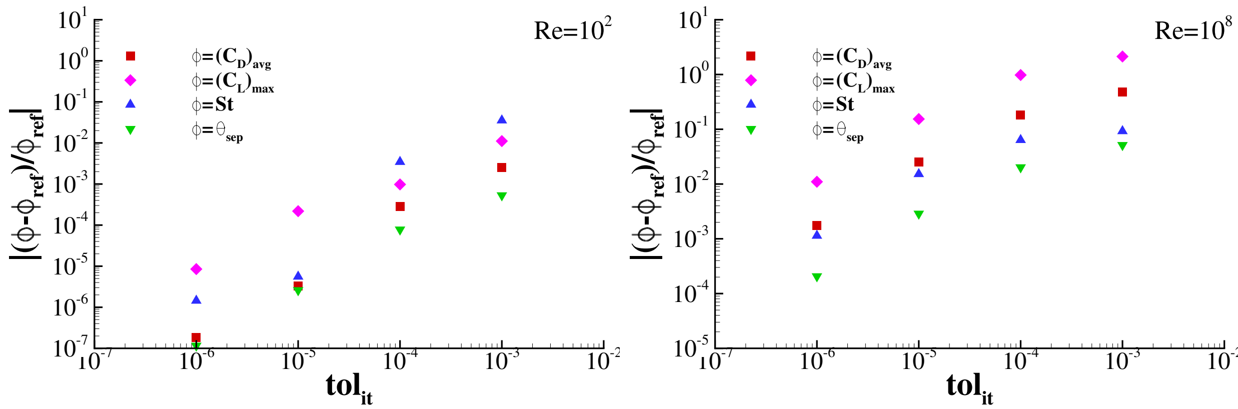

Figure 7: Time-averaged drag coefficient $(C_D)_{\mathrm{avg}}$, maximum lift coefficient $(C_L)_{\max}$, Strouhal number St and flow separation angle on the upper surface of the cylinder θ_{sep} as a function of the iterative convergence criteria tol_{it}. ϕ_{ref} is obtained with $tol_{\mathrm{it}} = 10^{-7}$. Calculation of the two-dimensional flow around a circular cylinder at Reynolds numbers of $Re = 10^2$ (laminar flow) and $Re = 10^8$ (SST $k{-}\omega$ turbulence model).

Naturally, it is not feasible to test the level of tol_{it} for all the flow settings considered in this study. Therefore, we have selected the 2D simulations at $Re = 10^2$ and $Re = 10^8$ using the SST turbulence model to address the contribution of iterative errors to the numerical uncertainty of the simulations.

Figure 7 presents the time-averaged drag coefficient $(C_D)_{\mathrm{avg}}$, the maximum lift coefficient $(C_L)_{\max}$, the Strouhal number St and the flow separation angle on the upper surface of the cylinder θ_{sep} as a function of tol_{it} for the 2D simulations performed for $r_i = 1$. It is clear that iterative convergence has a significant influence on the numerical accuracy of unsteady flow simulations performed with implicit time integration. The trends observed in the data are similar for the two Reynolds numbers. However, the level of iterative error for the same value of tol_{it} is significantly larger for $Re = 10^8$ than for $Re = 10^2$.

Naturally, the number of non-linear iterations performed at each time step N_{it} increases with the decrease of tol_{it}. For both cases illustrated in figure 7, $N_{\mathrm{it}} \simeq 5$ for $tol_{\mathrm{it}} = 10^{-3}$. For $tol_{\mathrm{it}} = 10^{-7}$, $N_{\mathrm{it}} \simeq 35$ for $Re = 10^2$ and $N_{\mathrm{it}} \simeq 100$ for $Re = 10^8$. This means that the computing time required to perform these unsteady flow simulations is extremely dependent on the choice of tol_{it}, especially for the highest Reynolds numbers. In the present study we have used $tol_{\mathrm{it}} = 10^{-6}$ for all simulations. In some cases, more than 100 iterations are performed at each time step. A consequence of this choice is that the two finest grids were not used for the 3D simulations due to the computer requirements to perform them. As an example, a calculation for $Re = 10^5$ and $r_i = 0.67$ with the SST model using 600 processors would require approximately 120 clock hours. However, it would not make sense to perform grid/time refinement studies with a less demanding iterative convergence criteria because the solution would be contaminated by iterative errors.

5.2.3 Discretization Errors

In well controlled simulations, the discretization errors should be the dominant contribution to the numerical uncertainty. As discussed in the previous sections, round-off and iterative errors should be negligible when compared to the discretization error. In most cases considered in this study, statistical errors will also be negligible when compared to the discretization errors. However, for the flow settings that lead to time histories with a wide range of frequencies (discussed below), it is likely that statistical errors are not negligible.

To illustrate the level of the contribution of the discretization errors to the numerical uncertainty we have selected three quantities of interest: the time-averaged drag coefficient $(C_D)_{\mathrm{avg}}$, the Strouhal number St and the time-averaged flow separation angle on the upper surface of the cylinder (θ_{sep}), which is determined at $z = 0.5L = 1.67D$ and from the transvered averaged solution. The method presented in [17] is used to estimate the numerical uncertainty using the 4 data points with the smallest values of r_i.

Figure 8 presents the results obtained for the laminar flow at $Re = 10^2$. For the same level of grid

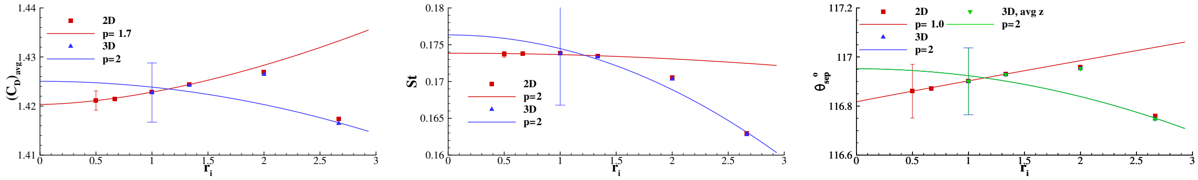

Figure 8: Grid/time convergence of the time-averaged drag coefficient $(C_D)_{\text{avg}}$, Strouhal number St and flow separation angle on the upper surface of the cylinder θ_{sep}. avg z designates transverse averaging. Calculation of the flow around a circular cylinder at a Reynolds number of $Re = 10^2$ (laminar flow).

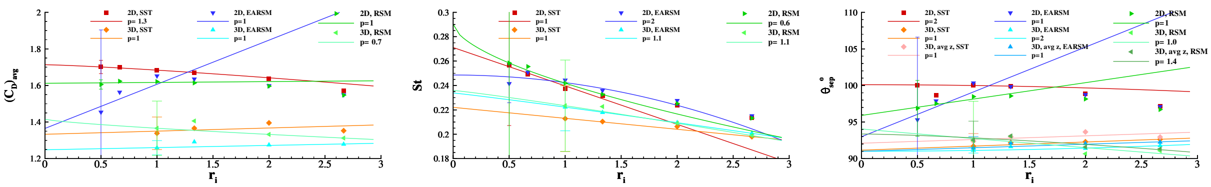

Figure 9: Grid/time convergence of the time-averaged drag coefficient $(C_D)_{\text{avg}}$, Strouhal number St and flow separation angle on the upper surface of the cylinder θ_{sep}. avg z designates transverse averaging. Calculation of the flow around a circular cylinder at a Reynolds number of $Re = 3.9 \times 10^3$ with RANS using the SST, EARSM and RSM turbulence models.

refinement, the 2D and 3D results are nearly identical. Furthermore, in the 3D simulations, θ_{sep} at $z = 0.5L = 1.67D$ is identical to the value obtained from the transverse averaged solution. The grid/time step with $r_i = 2.67$ is too coarse and its use in the numerical uncertainty estimation leads to a significant increase of the estimated numerical uncertainties. The estimated uncertainties for the 2D calculations performed with $r_i = 0.5$ are 0.14% for $(C_D)_{\text{avg}}$, 0.23 % for St and 0.094% for θ_{sep}.

The grid/time convergence properties of $(C_D)_{\text{avg}}$, St and θ_{sep} obtained for $Re = 3.9 \times 10^3$ with the SST, EARSM and RSM turbulence models are illustrated in figure 9. The main trends observed in the data are:

- The 2D simulations lead to larger values of $(C_D)_{\text{avg}}$ than the 3D calculations with differences that cannot be justified by the numerical uncertainty for the SST and RSM models. The 2D EARSM results obtained with $r_i < 1$ show a significantly different trend from the four coarsest grids and so a large numerical uncertainty of 31% is estimated. Numerical uncertainties estimated for the 3D simulations range from 3.1% for the EARSM model to 11.% for the RSM model;

- The Strouhal numbers of the 3D simulations are smaller than those obtained in 2D, but the estimated numerical uncertainties are larger than the differences between 2D and 3D simulations. For $r_i = 1$, the linear fits to the 3D data still indicate a numerical uncertainty of approximately 13% for SST, 8.7% for EARSM and 17% for RSM. The difference between the estimated uncertainties for EARSM and RSM reflects the scatter obtained for the RSM data. On the other hand, the 2D simulations performed for $r_i < 1$ do not show the same convergence behaviour of the four coarsest grids. In particular, the simulations performed with the SST model lead to a time-averaged asymmetric field that was not obtained with $r_i \geq 1$;

- The grid/time convergence properties of θ_{sep} are similar to those obtained for St with most 3D simulations leading to first-order fits to the data. The results obtained at $z = 0.5L = 1.67D$ are not equal to the transverse averaged data (avg z in the plots), but the differences are much smaller than the estimated numerical uncertainties, which range between 0.41% for EARSM and 5.8% for RSM. The results obtained for the EARSM 3D solutions show that small disturbances to the data can change the best fit to the data from first to second order. Therefore, in the presence of scatter in the data, the observed order of grid/time refinement must be interpreted carefully.

Figure 10 presents the grid/time convergence of $(C_D)_{\text{avg}}$, St and θ_{sep} for the simulations performed with the SST, EARSM and RSM models at $Re = 10^5$. In general, the convergence properties are smoother than

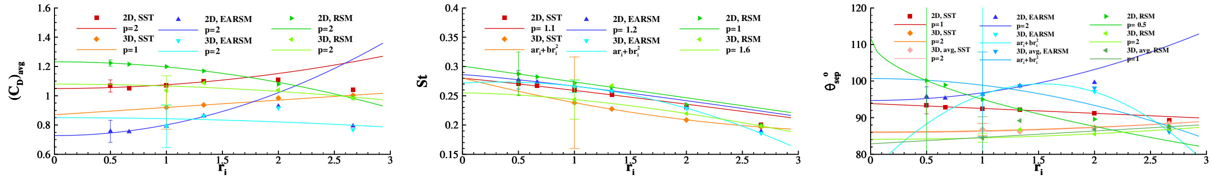

Figure 10: Grid/time convergence of the time-averaged drag coefficient $(C_D)_{\text{avg}}$, Strouhal number St and flow separation angle on the upper surface of the cylinder θ_{sep}. avg z designates transverse averaging. Calculation of the flow around a circular cylinder at a Reynolds number of $Re = 10^5$ with RANS using the SST, EARSM and RSM turbulence models.

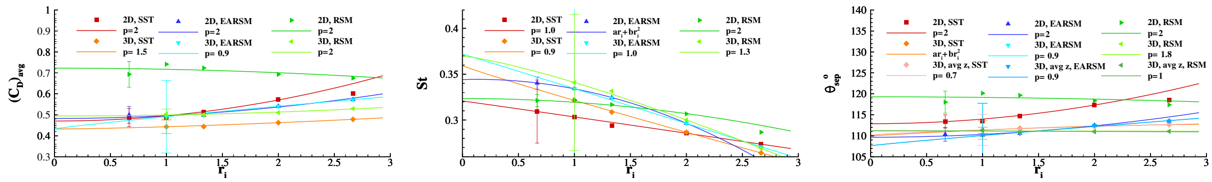

Figure 11: Grid/time convergence of the time-averaged drag coefficient $(C_D)_{\text{avg}}$, Strouhal number St and flow separation angle on the upper surface of the cylinder θ_{sep}. avg z designates transverse averaging. Calculation of the flow around a circular cylinder at a Reynolds number of $Re = 3.6 \times 10^6$ with RANS using the SST, EARSM and RSM turbulence models.

those obtained for $Re = 3.9 \times 10^3$ with all 2D simulations leading to symmetric time-averaged flow fields.

- For the EARSM model, the 2D and 3D simulations are surprisingly similar with the results obtained for $r_i \geq 2$ exhibiting non monotonic convergence. The numerical uncertainties estimated for the 2D simulations with $r_i = 0.5$ are 10% for $(C_D)_{\text{avg}}$, 5.7 % for St and 2.8% for θ_{sep};

- The SST model leads to lower values of $(C_D)_{\text{avg}}$ and θ_{sep} in the 3D simulations than in the 2D simulations that can hardly be justified by the numerical uncertainty. On the other hand, the differences between the 2D and 3D St decrease with grid/time refinement and so it is not clear if they will converge to different values;

- The largest differences between 2D and 3D results are obtained for the RSM model that also leads to the largest amount of scatter in the data, especially for the 3D simulations. The differences between θ_{sep} at $z = 0.5L = 1.67D$ and the transverse averaged θ_{sep} are also larger for the RSM results than for SST and EARSM data.

Grid/time convergence properties of $(C_D)_{\text{avg}}$, St and θ_{sep} for the simulations at $Re = 3.6 \times 10^6$ are presented in figure 11. There are similarities between the grid/time convergence properties obtained at $Re = 3.6 \times 10^6$ and those discussed above for $Re = 10^5$, especially for the EARSM model. Nonetheless, there are a few differences between the two Reynolds numbers for the results obtained with the SST and RSM models.

- $(C_D)_{\text{avg}}$ is smaller for 3D than for 2D and for the RSM model the difference is significantly larger than the estimated numerical uncertainties;

- For the SST and RSM models, the St of the 3D simulations shows a larger dependence on the grid/time refinement than the St obtained for two-dimensional flow. For the 3D results the estimated numerical uncertainties are 23% for the SST and 22% for the RSM model, whereas for the 2D simulations the St exhibits 11% (SST) and 2% (RSM) of numerical uncertainty.

Figure 12 presents the grid/time convergence properties of the three selected quantities of interest for the highest Reynolds number tested, $Re = 10^8$. The data does not exhibit the same trends of $Re = 10^5$ and $Re = 3.6 \times 10^6$ with the EARSM model leading to different results in 2D and 3D simulations.

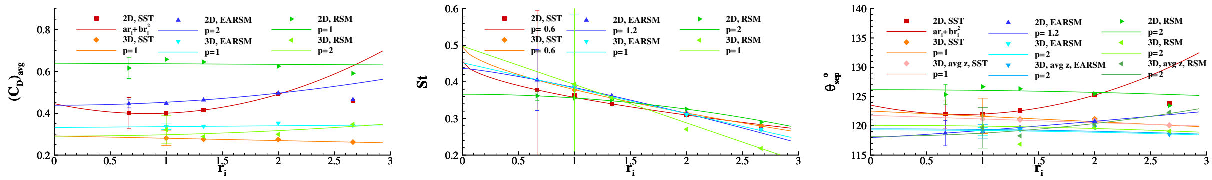

Figure 12: Grid/time convergence of the time-averaged drag coefficient $(C_D)_{\mathrm{avg}}$, Strouhal number St and flow separation angle on the upper surface of the cylinder θ_{sep}. avg z designates transverse averaging. Calculation of the flow around a circular cylinder at a Reynolds number of $Re = 3.6 \times 10^6$ with RANS using the SST, EARSM and RSM turbulence models.

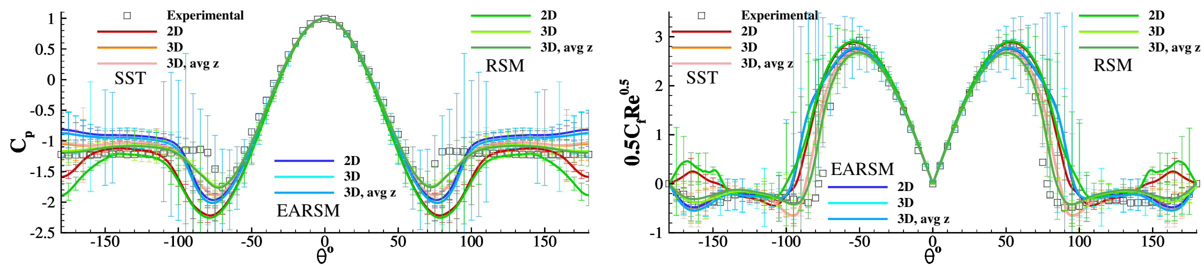

Figure 13: Time averaged pressure C_p and skin friction C_f coefficients on the cylinder surface obtained in the 2D and 3D simulations with RANS using the SST, EARSM and RSM turbulence models. Experimental data from [5]. Flow around a circular cylinder at a Reynolds number of $Re = 10^5$.

- The time-averaged drag coefficient $(C_D)_{\mathrm{avg}}$ obtained in the 2D simulations is larger than $(C_D)_{\mathrm{avg}}$ of the 3D simulations for the three turbulence models tested. The numerical uncertainties are smaller than the discrepancies between the 2D and 3D results and the RSM models exhibits the largest amount of scatter in the data;

- There is a large grid/time dependency for the St number obtained in the 2D and 3D simulations of the three turbulence models, with the exception of the RSM data in 2D that exhibits a numerical uncertainty of 3.5% for $r_i = 0.67$. With the estimated level of numerical uncertainty, it is not possible to quantify discrepancies between the St obtained in 2D and 3D calculations;

- With the SST and EARSM models, θ_{sep} is similar for the 2D and 3D simulations, whereas the RSM model exhibits a larger value of θ_{sep} for 2D than for 3D with a difference that is not justified by the numerical uncertainty.

5.3 Comparison with Experimental Data

Experimental measurements of the time-averaged pressure C_p and skin friction C_f coefficients on the cylinder surface are reported in [5] for $Re = 10^5$ and $Re = 3.6 \times 10^6$. Figure 13 presents the comparison of the time-averaged C_p and C_f distributions obtained in the 2D and 3D simulations with RANS using the SST, EARSM and RSM models with the experimental data for $Re = 10^5$, whereas the same comparison at $Re = 3.6 \times 10^6$ is presented in figure 14. The plots are inlcude the estimated error bars for the simulations results. Four grids are used to estimate the error bars plotted in figures 13 and 14. 3D solutions are obtained in the $r_i = 1$ grids, whereas 2D results are obtained in the $r_i = 0.5$ grids for $Re = 10^5$ and $r_i = 0.67$ for $Re = 3.6 \times 10^6$.

At $Re = 10^5$, experiments exhibit laminar flow separation at $\theta_{\mathrm{sep}} = \pm 78°$, whereas all simulations exhibit $|\theta_{\mathrm{sep}}| > 90°$ because transition to turbulent flow occurs upstream of separation. This is an expected result, because RANS turbulence models predict transition to turbulent flow at unreasonably small Reynolds

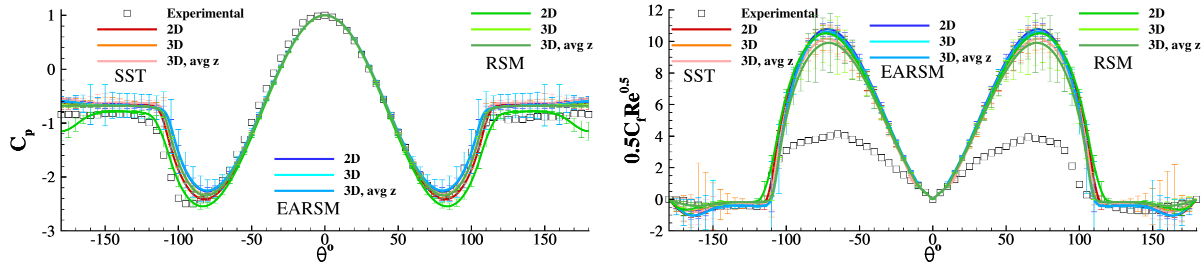

Figure 14: Time averaged pressure C_p and skin friction C_f coefficients on the cylinder surface obtained in the 2D and 3D simulations with RANS using the SST, EARSM and RSM turbulence models. Experimental data from [5]. Flow around a circular cylinder at a Reynolds number of $Re = 3.6 \times 10^6$.

numbers [21]. Nonetheless, the results closest to the experiments are obtained in the 3D RSM simulations. On the other hand, the 2D RSM and SST simulations lead to an awkward result with $C_f > 0$ in the near-wake that is not obtained for the EARSM.

The reported location of transition to turbulent flow at $Re = 3.6 \times 10^6$ is $\theta = \pm 65°$ that is again downstream of the location obtained in the simulations which is close to approximately $\theta = \pm 20°$. As a consequence there is a significant discrepancy between the experimental C_f and the results of the simulations in the region of attached flow. However, for this super-critical Reynolds number with turbulent flow separation the differences between experiments and simulations are clearly smaller than those obtained for the sub-critical Reynolds number of 10^5. Furthermore, the differences between the six simulations at $Re = 3.6 \times 10^6$ are also significantly smaller than those obtained at $Re = 10^5$.

For both quantities, C_p and C_f, the estimated error bars tend to be larger for $Re = 10^5$ than for $Re = 3.6 \times 10^6$. Nonetheless, for the present level of grid/time refinement, numerical uncertainties are only negligible for the C_p distribution on the attached flow region.

5.4 Is it RANS?

One of the goals of this study is to investigate if the turbulence models provide enough diffusion to guarantee that the dependent variables correspond to the mean flow quantities. To this end we have calculated the frequency content of the time signals of the lift coefficient C_L and of the mean horizontal velocity component V_x for point P_1 located at $(x = 0.75D, y = 0.4D, z = 1.67D)$ using the fast Fourier transform tool of TecPlot [22].

Figure 15 illustrates the results obtained with the SST turbulence model for the four Reynolds numbers tested. All the 2D simulations lead to the expected behavior of RANS simulations with discrete frequencies appearing in the time histories of C_L and V_x for all grid/time refinement levels. However, for the 3D simulations the scenario is not the same. Time histories of V_x at P_1 show a wide range of frequencies that are not expected in a RANS simulation. These frequencies do not appear for $r_i = 2$ and $r_i = 2.67$ for $Re = 3.9 \times 10^3$ and the results at the highest Reynolds number tested $Re = 10^8$ are those that are closest to the expected behavior. For all Reynolds numbers, amplitude of the C_L oscillations are larger in the 2D simulations than in the 3D results.

The results obtained with the EARSM turbulence model are illustrated in figure 16. The trends observed in the data are not identical to those obtained for the SST turbulence model. All simulations exhibit the expected frequency content of C_L and V_x at P_1. On the other hand, the differences between 2D and 3D simulations are smaller than those obtained for the SST model and tend to decrease with the increase of the Reynolds number.

Figure 17 presents the time histories of C_L and V_x at P_1 and its frequency content for the simulations performed with the RSM model. The results show the largest differences between the 2D and 3D simulations that tend to grow with the increase of the Reynolds number, which is exactly the opposite trend of that observed for the EARSM data. However, in the RSM 3D simulations the frequency content of the time histories of V_x at P_1 are not typical of RANS simulations. For $Re \leq 3.6 \times 10^6$, the range of frequencies

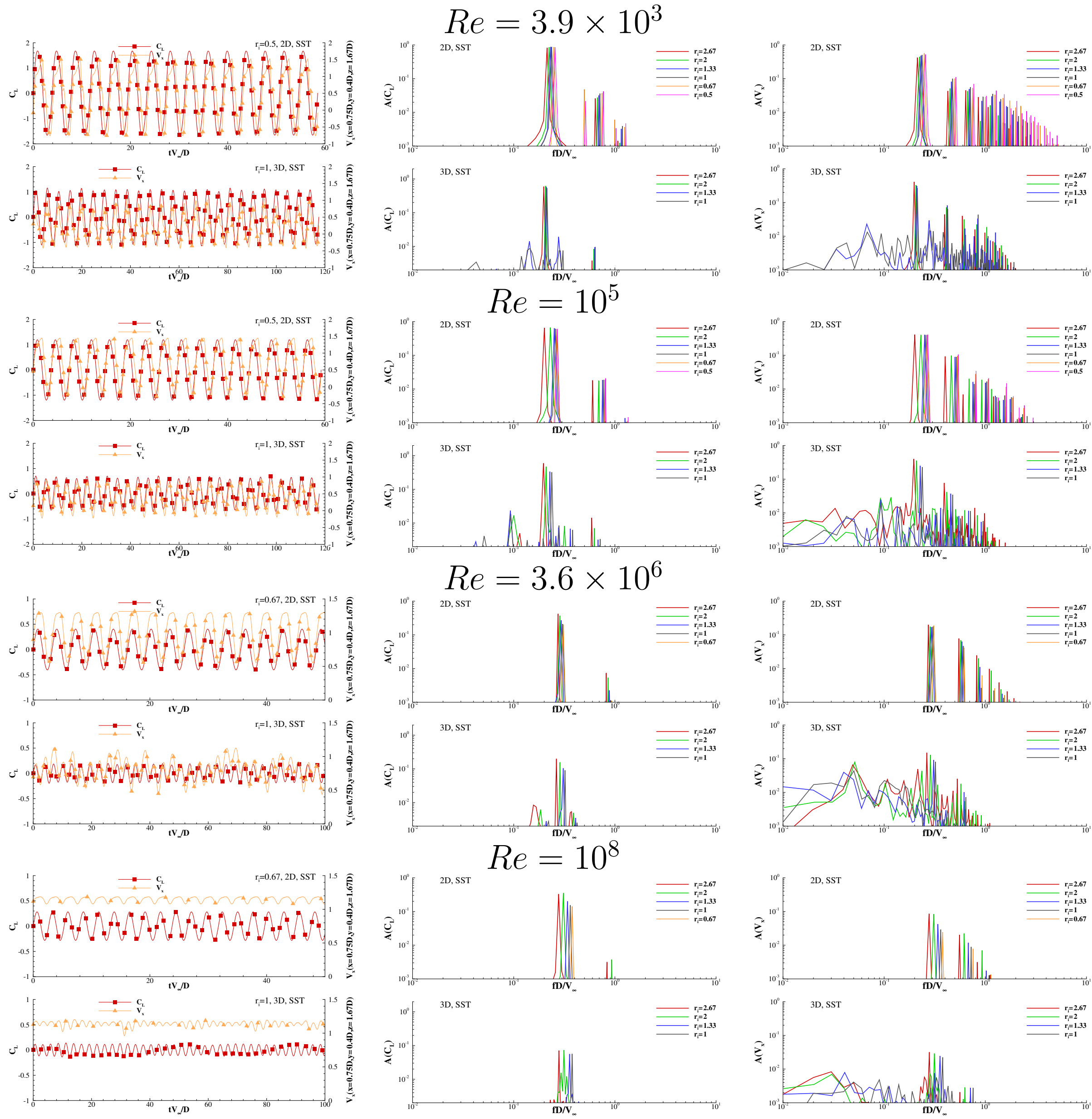

Figure 15: Time-histories and frequency content of the lift coefficient C_L and mean horizontal velocity component V_x for point P_1 located at $(x = 0.75D, y = 0.4D, z = 1.67D)$ obtained in the 2D and 3D simulations with RANS using the SST turbulence model.Flow around a circular cylinder at different Reynolds numbers.

present in the V_x time history tends to increase with grid/time refinement, whereas the opposite trend is observed at $Re = 10^8$.

Naturally, for all the simulations that exhibit a wide range of frequencies in the time history of V_x at P_1, statistical convergence is not as good as that obtained for the other cases.

To analyse the differences between the results obtained with the different turbulence models at the selected Reynolds numbers, we have calculated the time-averaged isolines of V_x at $z = 1.67D$ and the effective Reynolds number,

$$Re_{\mathrm{ef}} = \frac{V_\infty D}{\nu + \nu_t} \; .$$

Naturally, the RSM model does not use ν_t to determine the Reynolds stresses. However, ν_t is calculated

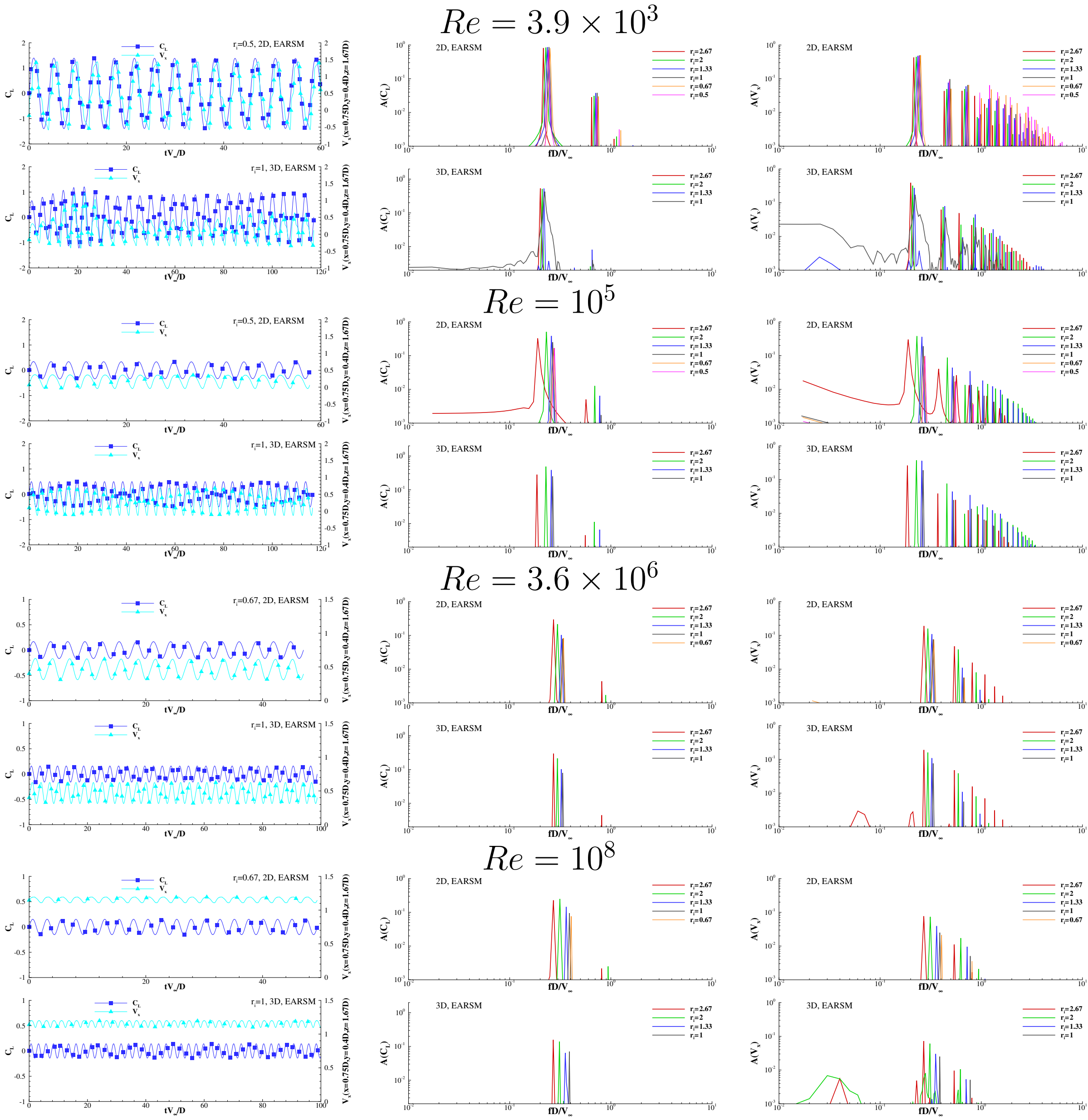

Figure 16: Time-histories and frequency content of the lift coefficient C_L and mean horizontal velocity component V_x for point P_1 located at $(x = 0.75D, y = 0.4D, z = 1.67D)$ obtained in the 2D and 3D simulations with RANS using the EARSM turbulence model.Flow around a circular cylinder at different Reynolds numbers.

from k and ω to solve the ω transport equation.

Figures 18 (2D) and 19 (3D) present the results obtained for $Re = 3.9 \times 10^3$. The flow field in the near-wake of the 2D simulations are awkward with only very small regions of negative V_x (indicated by the white region in the plots). As reported in [9], V_x should remain negative for $\theta > \theta_{\text{sep}}$. This result is most likely a consequence of the level of ν_t obtained in the near-wake region. The fields of Re_{ef} obtained with the three turbulence models in 3D are more similar than those obtained in 2D. Furthermore, the EARSM model leads to the smallest differences between the Re_{ef} fields of 2D and 3D simulations. There is still a narrow region of positive V_x in the near-wake of the 3D RSM simulation. However, this region should disappear with grid time/refinement because it is significantly smaller in the $r_i = 1$ calculation than in the $r_i = 1.33$

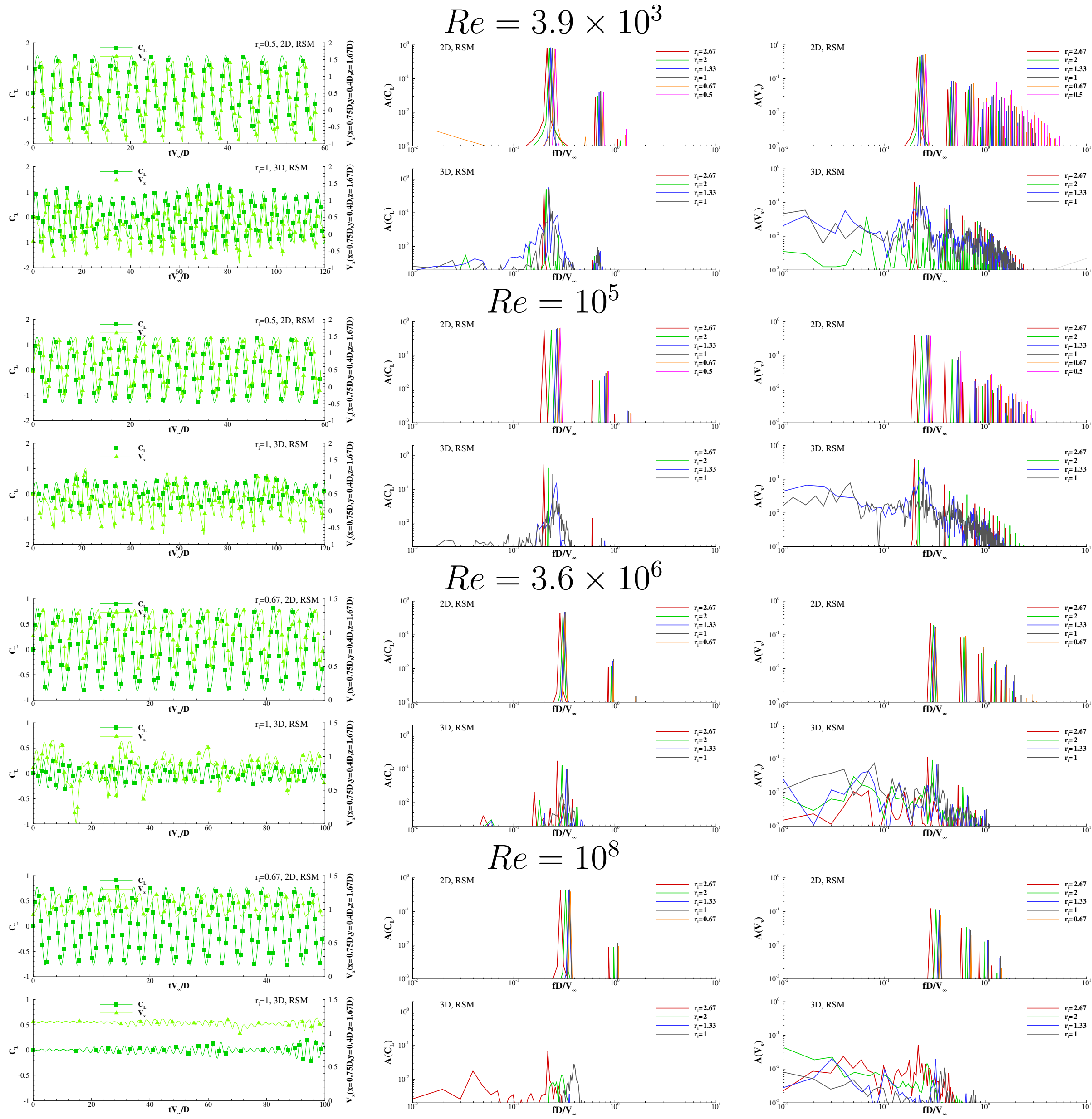

Figure 17: Time-histories and frequency content of the lift coefficient C_L and mean horizontal velocity component V_x for point P_1 located at $(x = 0.75D, y = 0.4D, z = 1.67D)$ obtained in the 2D and 3D simulations with RANS using the RSM turbulence model.Flow around a circular cylinder at different Reynolds numbers.

results, which are not included in figure 19.

The results obtained at $Re = 10^5$ are depicted in figures 20 (2D) and 21 (3D). The 2D simulations that are more similar to the 3D results are again obtained with the EARSM model. For this condition, only the RSM model still shows a small region with positive values of V_x in the near-wake, which should not be observed in the near-wake field [23]. These awkward wakes are obtained for the highest levels of Re_{ef} in the near-wake, which is equivalent to the lowest levels of ν_t. The 3D results obtained with the three turbulence models are a lot more similar than those obtained at $Re = 3.9 \times 10^3$. At this Reynolds number, the main shortcoming of the RANS turbulence models is the early onset of transition.

Figures 22 (2D) and 23 (3D) present the results obtained at $Re = 3.6 \times 10^6$. The trends are very similar to those obtained for $Re = 10^5$. Nonetheless, the 2D RSM solution does not exhibit positive values of V_x in

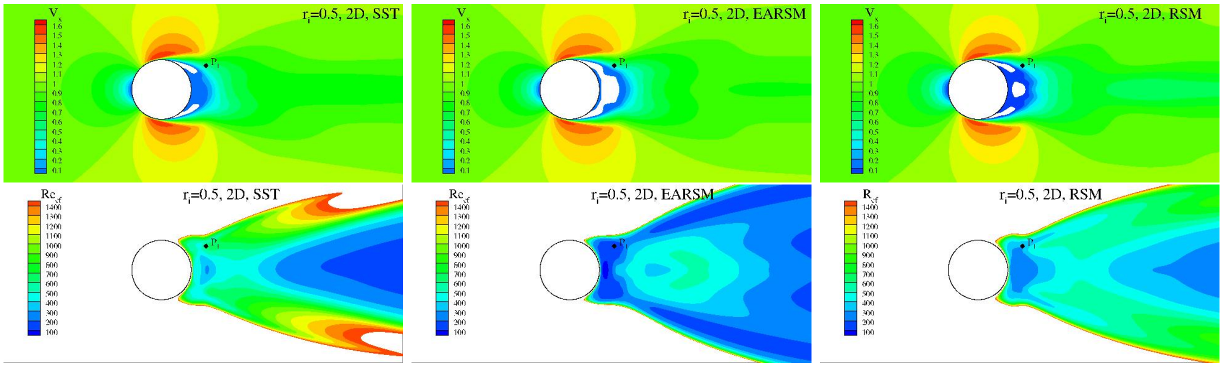

Figure 18: Isolines of the time averaged mean horizontal velocity component V_x at $z = 1.67D$ obtained in the 2D simulations with RANS using the SST, EARSM and RSM turbulence models. White regions correspond to $V_x < 0$ and $Re_{\mathrm{ef}} > 1500$. Flow around a circular cylinder at a Reynolds number of $Re = 3.9 \times 10^3$.

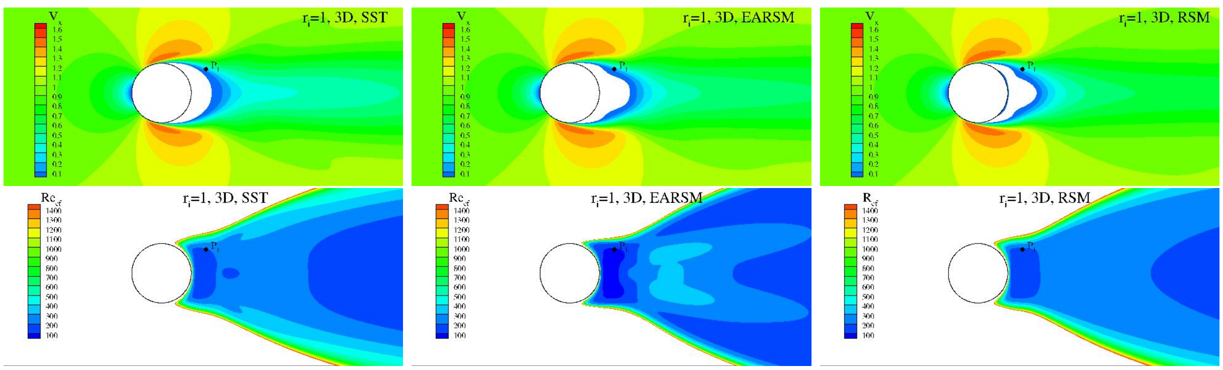

Figure 19: Isolines of the time averaged mean horizontal velocity component V_x at $z = 1.67D$ obtained in the 3D simulations with RANS using the SST, EARSM and RSM turbulence models. White regions correspond to $V_x < 0$ and $Re_{\mathrm{ef}} > 1500$. Flow around a circular cylinder at a Reynolds number of $Re = 3.9 \times 10^3$.

the near-wake. However, the largest differences between 2D and 3D simulations are again obtained for the RSM model.

Finally, figures 24 (2D) and 25 (3D) present the results obtained at the highest Reynolds number selected, $Re = 10^8$. The data exhibits the same trends observed for $Re = 3.6 \times 10^6$, but for the 3D simulations the

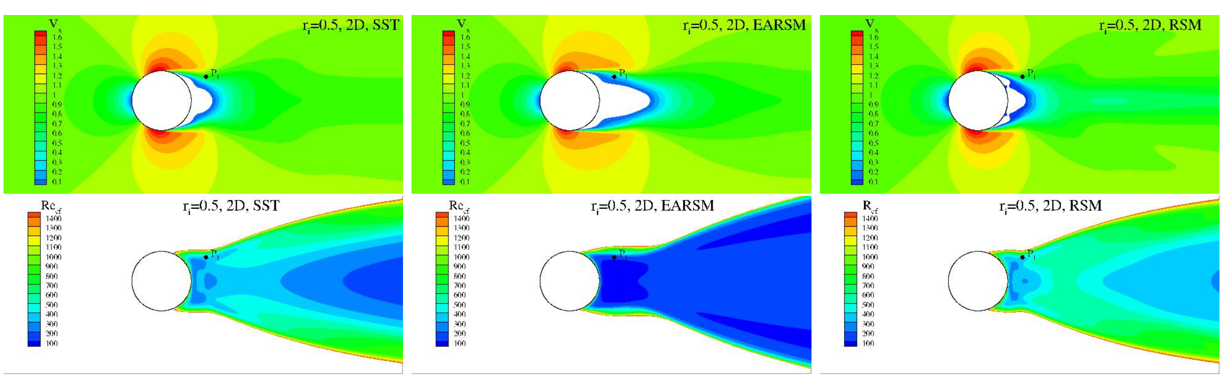

Figure 20: Isolines of the time averaged mean horizontal velocity component V_x at $z = 1.67D$ obtained in the 2D simulations with RANS using the SST, EARSM and RSM turbulence models. White regions correspond to $V_x < 0$ and $Re_{\mathrm{ef}} > 1500$. Flow around a circular cylinder at a Reynolds number of $Re = 10^5$.

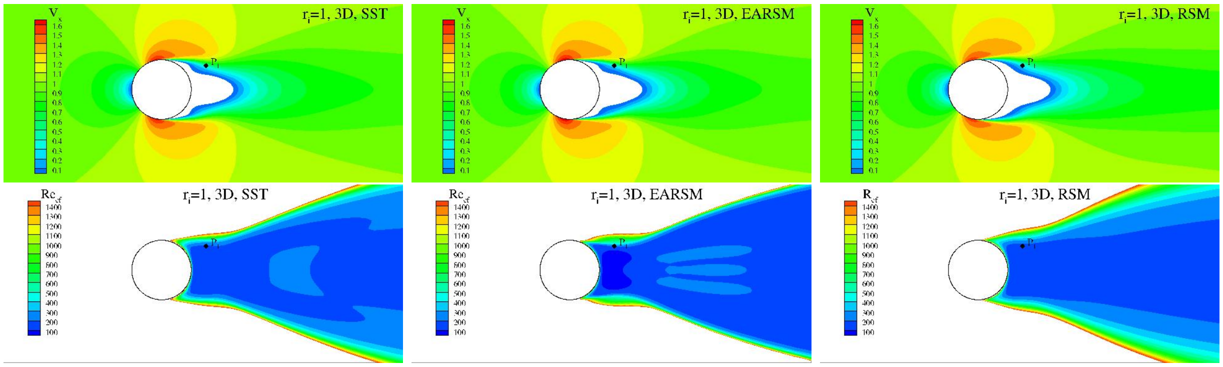

Figure 21: Isolines of the time averaged mean horizontal velocity component V_x at $z = 1.67D$ obtained in the 3D simulations with RANS using the SST, EARSM and RSM turbulence models. White regions correspond to $V_x < 0$ and $Re_{\mathrm{ef}} > 1500$. Flow around a circular cylinder at a Reynolds number of $Re = 10^5$.

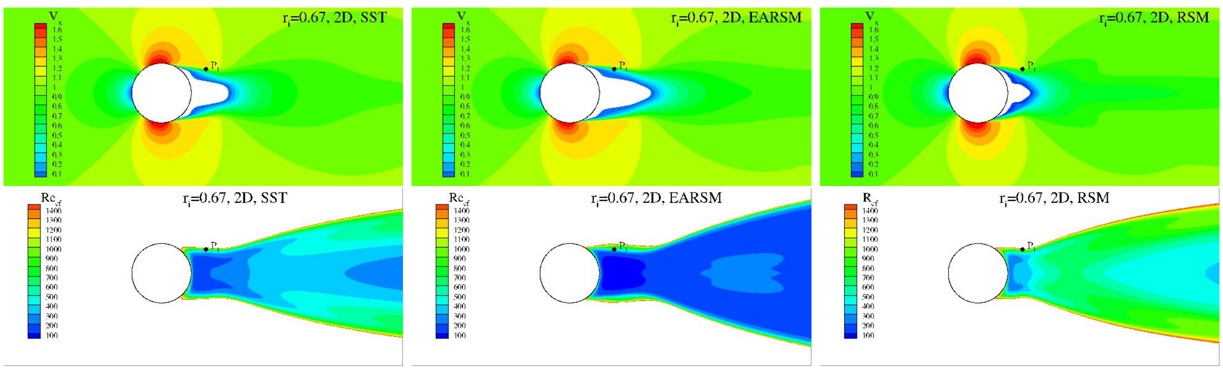

Figure 22: Isolines of the time averaged mean horizontal velocity component V_x at $z = 1.67D$ obtained in the 2D simulations with RANS using the SST, EARSM and RSM turbulence models. White regions correspond to $V_x < 0$ and $Re_{\mathrm{ef}} > 1500$. Flow around a circular cylinder at a Reynolds number of $Re = 3.6 \times 10^6$.

discrepancies between the three turbulence models solutions are the smallest of all Reynolds numbers tested. To conclude, the results obtained with the EARSM model in 2D and 3D are remarkably similar for the currently tested Reynolds numbers. The RSM model in 2D shows a too short recirculation area in the near-wake for all Reynolds numbers, whereas the SST results are in between the RSM and EARSM solutions. In 3D, the differences between the flow fields obtained with the three turbulence models are much smaller than in 2D.

6 Conclusions

This paper presents a study on the numerical simulation of statistically unsteady turbulent flows using the RANS equations. Calculations are performed for the SST $k{-}\omega$ eddy-viscosity model, a $k{-}\omega$ based explicit algebraic Reynolds stress model (EARSM) and a Reynolds stress model (RSM) that uses the ω equation to determine the dissipation rate of Reynolds stresses (SSG/LRR$-\omega$). The selected test case is the flow around a circular cylinder at four Reynolds numbers: $Re = 3.9 \times 10^3$, $Re = 10^5$, $Re = 3.6 \times 10^6$ and 10^8. Simulations are performed with a second-order incompressible flow solver in two-dimensional (2D) and three-dimensional (3D) geometries. Dimensions of the computational domain were selected according to available experimental data in [5]. Preliminary calculations were performed for the 2D and 3D geometries at $Re = 100$ that corresponds to laminar flow.

Two main topics are addressed in this investigation: the numerical uncertainty of unsteady flow sim-

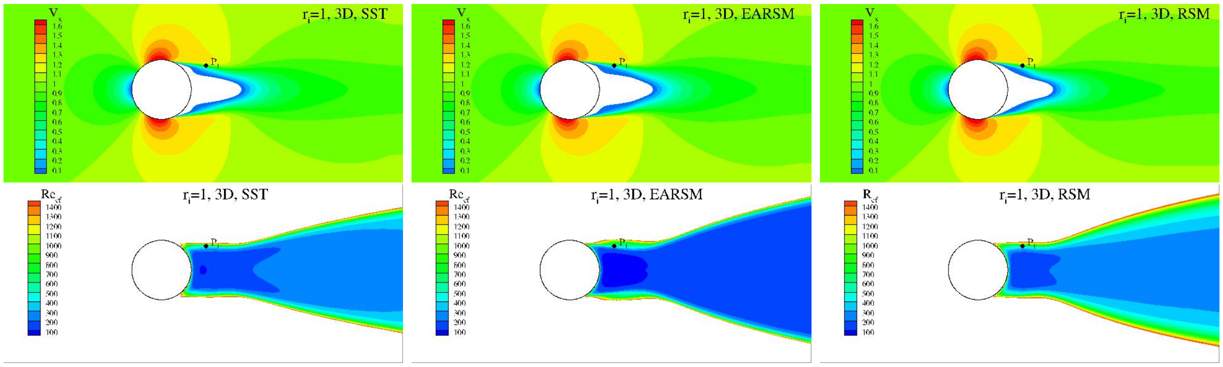

Figure 23: Isolines of the time averaged mean horizontal velocity component V_x at $z = 1.67D$ obtained in the 3D simulations with RANS using the SST, EARSM and RSM turbulence models. White regions correspond to $V_x < 0$ and $Re_{\text{ef}} > 1500$. Flow around a circular cylinder at a Reynolds number of $Re = 3.6 \times 10^6$.

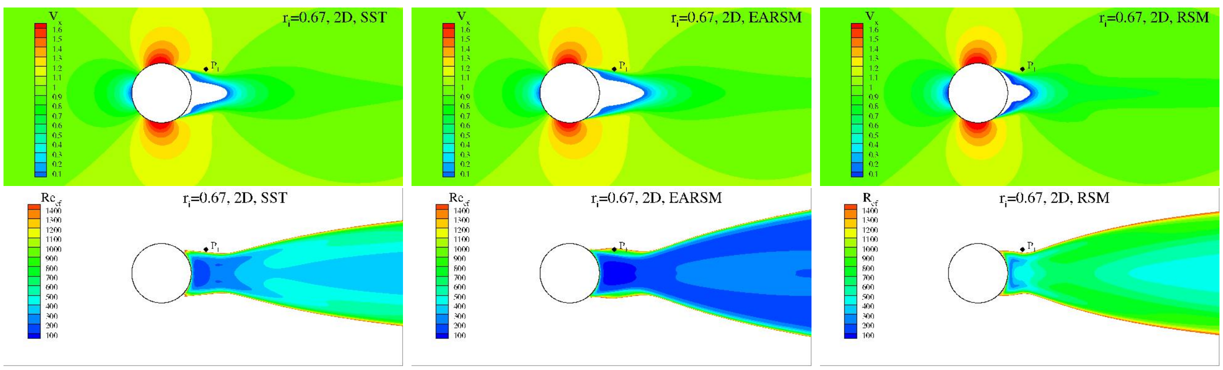

Figure 24: Isolines of the time averaged mean horizontal velocity component V_x at $z = 1.67D$ obtained in the 2D simulations with RANS using the SST, EARSM and RSM turbulence models. White regions correspond to $V_x < 0$ and $Re_{\text{ef}} > 1500$. Flow around a circular cylinder at a Reynolds number of $Re = 10^8$.

ulations and the assessment if the computed solution corresponds to the mean flow quantities. The first topic includes the estimation of statistical, iterative and discretization errors using grid/time refinements studies. The frequency content of the time histories of force coefficients and mean velocity components in the near-wake is determined to check if only discrete frequencies are present.

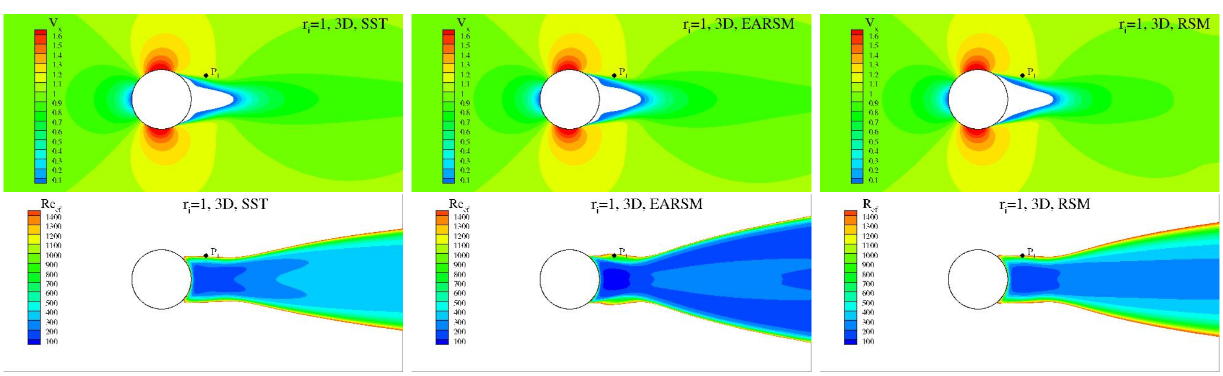

Figure 25: Isolines of the time averaged mean horizontal velocity component V_x at $z = 1.67D$ obtained in the 3D simulations with RANS using the SST, EARSM and RSM turbulence models. White regions correspond to $V_x < 0$ and $Re_{\text{ef}} > 1500$. Flow around a circular cylinder at a Reynolds number of $Re = 10^8$.

The main conclusions of this study are:

- For similar levels of grid refinement on the cylinder surface (number of cell faces on the cylinder surface) the numerical uncertainty of all RANS simulations are at least one order of magnitude larger than that obtained for the laminar flow;
- More demanding iterative convergence criteria than what is usually seen in the open literature are required to obtain negligible contributions of the iterative error;
- Statistical convergence is strongly dependent on the frequency content of the flow dependent variables and so the two topics addressed in this study are linked;
- Two-dimensional simulations with the three selected turbulence models always lead to "RANS-like" time histories of the dependent variables. However, some of the computed results in the near-wake of the cylinder are physically unacceptable:
  - For the SST and EARSM models, only the $Re = 3.9 \times 10^3$ solutions exhibit near-wakes with positive streamwise velocities. However, the differences between 2D and 3D simulations are larger for the SST model than for the EARSM model that leads to remarkably similar results for all Reynolds number.
  - The RSM model does not perform well in 2D simulations. There is a significant difference between the 2D and 3D simulations for all the Reynolds numbers tested;
- For the 3D simulations, the EARSM leads to "RANS-like" solutions for all Reynolds numbers tested. On the other hand, most of the simulations performed with the RSM model lead to a wide range of frequencies in the time histories of the flow mean dependent variables. Nonetheless, this phenomena seems to decrease with the increase of the Reynolds number. However, the narrowing of the wake with the increase of the Reynolds number can influence this result;
- The differences between the 3D simulations performed with the three turbulence models decrease with the increase of the Reynolds number.

This study also includes the comparison of time averaged pressure and skin-friction coefficients on the cylinder surface with experimental data available in the literature. Most of the discrepancies obtained are a consequence of a well-known shortcoming of RANS turbulence models: the determination of the onset of transition to turbulent flow.

References

[1] D. C. Wilcox. *Turbulence Modeling for CFD.* 2$^{\mathrm{nd}}$ Edition, DCW Industries, Inc., 2006.

[2] F. R. Menter, M. Kuntz, R. Langtry, Y. Nagano, M. J. Tummers, and K. Hanjalic. Ten years of industrial experience with the sst turbulence model, 4th:; internal symposium, turbulence, heat and mass transfer. In *4*$^{\mathrm{th}}$ *Internal Symposium, Turbulence, Heat and Mass Transfer*, volume 4, pages 625–632, New York, 2003. Begell House,;.

[3] A. Hellsten. New advanced $k - \omega$ turbulence model for high-lift aerodynamics. *AIAA Journal*, 43(9):1857–1869, 2005.

[4] B. Eisfeld, C. Rumsey, and V. Togiti. Verification and validation of a second-moment-closure model. *AIAA Journal*, 54(5):1524–1541, 2016.

[5] E. Achenback. Distribution of local pressure and skin friction around a circular cylinder in cross-flow up to $re = 5 \times 10^6$. *Journal of Fluid Mechanics*, 34(4):625–639, 1968.

[6] L. Eça, Vaz G., Toxopeus S.L., and M. Hoekstra. Numerical Errors in Unsteady Flow Simulations. *ASME Journal of Verification, Validation and Uncertainty Quantification*, 4(2):021001, 2019.

[7] American Society of Mechanical Engineers. *Standard for Verification and Validation in Computational Fluid Dynamics and Heat Transfer.* Normes ASME. American Society of Mechanical Engineers, 2009.

[8] M. M. Zdravkovich. *Flow Around Circular Cylinders Volume 1: Fundamentals.* Oxford University Press, 1997.

[9] F.S. Pereira, G. Vaz, and L. Eça. Evaluation of RANS and SRS methods for simulation of the flow around a circular cylinder in the sub-critical regime. *Ocean Engineering*, 186:106067, 2019.

[10] A. Maximiano, L. Eça, G. Vaz, and M. Alves. CFD analysis of different passive guiding system geometries on a semi-closed fish farm cage. In *12*th *World Congress of the RSAI – Regional Science Association International*, May 2018.

[11] L. Eça and M. Hoekstra. On the grid sensitivity of the wall boundary condition of the $k-\omega$ turbulence model. *Journal of Fluids Engineering*, 126(6):900–910, 03 2005.

[12] C. M. Klaij and C. Vuik. Simple-type preconditioners for cell-centered, collocated finite volume discretization of incompressible Reynolds-averaged Navier-Stokes equations. *International Journal for Numerical Methods in Fluids*, 71(7):830–849, 2013.

[13] T.F. Miller and F. W. Schmidt. Use of a pressure-weighted interpolation method for the solution of the incompressible navier-stokes equations on a nonstaggered grid system. *Numerical Heat Transfer*, 14(2):213–233, 1988.

[14] L. Eça, C.M. Klaij, G. Vaz, M. Hoekstra, and F.S. Pereira. On code verification of rans solvers. *Journal of Computational Physics*, 310:418–439, 2016.

[15] L. Eça, M. Hoekstra, and J. Windt. Practical grid generation tools with applications to ship hydrodynamics. In *8*th *International Conference on Numerical Grid Generation in Computational Field Simulations, Honolulu, Hawaii, U.S.A.*, 2002.

[16] M. Vinokur. On One-Dimensional Stretching Functions for Finite-Difference Calculations. *Journal of Computational Physics*, 50(2):215–234, 1983.

[17] L. Eça and M. Hoekstra. A procedure for the estimation of the numerical uncertainty of CFD calculations based on grid refinement studies. *Journal of Computational Physics*, 262:104–130, 2014.

[18] J. Brouwer, J. Tukker, Y. Klinkenberg, and M. van Rijsbergen. Random uncertainty of statistical moments in testing: Mean. *Ocean Engineering*, 182:563–576, 2019.

[19] J. Brouwer, J. Tukker, and M. van Rijsbergen. Uncertainty analysis of finite length measurement signals. In *5*th *International Conference on Advanced Model Measurement Technology for the Maritime Industry*, 09 2013.

[20] L. Eça, G. Vaz, M. Hoekstra, S. Pal, E. Muller, D. Pelletier, A. Bertinetti, R. Difonzo, L. Savoldi, R. Zanino, A. Zappatore, Y. Chen, K. J. Maki, H. Ye, J. Drofelnik, B. Moss, and A. Da Ronch. Overview of the 2018 workshop on iterative errors in unsteady flow simulations. *Journal of Verification, Validation and Uncertainty Quantification*, 5(2), August 2020. 021006.

[21] L. Eça and M. Hoekstra. The numerical friction line. *Journal of Marine Science and Technology*, 13(4):328–345, 2008.

[22] Tecplot 360. *User's Manual*. Tecplot Inc., 2021.

[23] F.S. Pereira, L. Eça, G. Vaz, and S.S. Girimaji. On the simulation of the flow around a circular cylinder at Re=140,000. *International Journal of Heat and Fluid Flow*, 76:40–56, 2019.